Commun. Comput. Phys.
doi: 10.4208/cicp.OA-2016-0212

Vol. **22**, No. 5, pp. 1258-1285
November 2017

The Modified Ghost Method for Compressible Multi-Medium Interaction with Elastic-Plastic Solid

Zhiwei Feng[1], Jili Rong[1,*], Abouzar Kaboudian[2] and Boo Cheong Khoo[3]

[1] *School of Aerospace Engineering, Beijing Institute of Technology, Beijing 100081, P.R. China.*
[2] *School of Physics, Georigia Institute of Technology, Atlanta GA 30332-0400, USA.*
[3] *Department of Mechanical Engineering, National University of Singapore, 5A Engineering Drive 1, 02-02, Singapore.*

Received 19 November 2016; Accepted (in revised version) 9 March 2017

Abstract. In this work, a robust, consistent, and coherent approach, termed as Modified Ghost Method (MGM), is developed to deal with the multi-medium interaction with elastic-plastic solid. This approach is simple to implement and keeps the solvers intact, and can handle multi-medium problems which involve various media including gas, liquid and solid. The MGM is first validated by two-dimensional (2D) cases and then is applied to study the interaction between elastic-plastic solid structure and the underwater explosion. The development of the wave system is described and analyzed. Furthermore, two kinds of complex solid structure subjected to underwater explosion are simulated. Finally, a complex solid structure immersed in water subjected to underwater explosion is simulated and analyzed. The numerical experiments show the viability, effectiveness and versatility of the proposed method which is able to accurately predict the wave pattern at various interfaces.

AMS subject classifications: 35Q31, 74F10, 74S20, 76T99

Key words: Multi-medium interaction, modified ghost method, elastic-plastic solid, complex solid structure.

1 Introduction

Fluid-structure interaction (FSI) includes numerous applications ranging from civil engineering [1], hemodynamics [2], the design process of bridges [3] and lightweight membrane structure [4] to submerged structure subjected to underwater explosion [5]. The numerical realization of coupling is classified by Schafer as weak or strong [6]. The term

*Corresponding author. *Email addresses:* 645219868@qq.com (Z. W. Feng), rongjili@bit.edu.cn (J. L. Rong), abouzar.kaboudian@gmail.com (A. Kaboudian) mpekbc@nus.edu.sg (B. C. Khoo)

 ©2017 Global-Science Press

https://doi.org/10.4208/cicp.OA-2016-0212 Published online by Cambridge University Press

"weak coupling" refers to the partitioned approaches where the solver for one physical field is explicitly independent of methods for other physical fields. The coupling is achieved by passing the force and displacement between the solvers back and forth and satisfying the interfacial conditions. However, the interfacial conditions have not been taken into account for to consider the wave refraction occurred at the interfaces, which may lead to unreasonable and inaccurate wave refraction at the interface. The strong coupling refers to monolithic approaches where the solver is extensively modified such that the unknowns are calculated simultaneously for all the fields by properly constructing the coupled equations. Some other methods that are not necessarily fully monolithic or fully-partitioned approaches, like immersed interface method [7], immersed boundary method [8], volume of fluid method [9] and phased-field method [10], have been developed to simulate the multi-medium problems. This means that the fields are decoupled using special techniques that will make the coupling more stable, and at the same time, satisfy the interfacial conditions as accurately as possible. In this work, the weak coupling strategy is chosen by the fact that we can use independent fluid and solid solver and the interaction is achieved by applying boundary condition at the interface. In order to achieve the interaction, Modified Ghost Fluid Method (MGFM) is further developed to deal with the 2D FSI problems with the elastic-plastic solid.

The Ghost Fluid Method (GFM) has been first proposed by Fedkiw [11] and named as original GFM (OGFM) to distinguish it from other modified versions. Since the OGFM appears to be rather problem related, to overcome the limitation, Liu et al. [12] proposed the modified GFM (MGFM) algorithm. Subsequent to that, the real GFM (RGFM) was developed by Wang et al. [13] The MGFM and RGFM have been successfully applied to different extreme cases of gas-gas, gas-water, and even fluid-elastic structure problems [14]. In this paper, we develop the MGFM so that it can deal with the 2D FSI with elastic-plastic solid. Very recently, Kaboudian et al. [15, 16] proposed the modified Ghost Solid Method (MGSM) based on the characteristic features of MGFM, which was applied to the solid-solid interaction problems where elastic-elastic, elastic-plastic and plastic-plastic deformations take place. To facilitate subsequent discussion, the MGFM and MGSM are conjunctively termed as the Modified Ghost Method (MGM). Thus, the truly multi-medium interaction problems involving various phases of material, namely fluid phase (liquid and gas) and solid phase, can be solved with the MGM, which is the main focus of this paper and leads to a consistent, robust, and coherent approach that can numerically model various interactions: liquid-liquid, gas-liquid, gas-gas, fluid-solid, solid-solid interactions. In this paper, as usual, structural equations are solved in a Lagrangian formulation and on the other hand, flow equations are solved in an Eulerian formulation.

The remainder of this paper is organized as follows. In Section 2, we describe the governing equations, the fundamental theory of plasticity for solid and the details about MGM for the 2D multi-medium interaction problems. In Section 3, several numerical experiments are carried out, which demonstrate the accuracy and corroboration of the MGM. Conclusions are provided in Section 4.

https://doi.org/10.4208/cicp.OA-2016-0212 Published online by Cambridge University Press

2 The MGM for 2D multi-medium interaction

2.1 Governing equations

2.1.1 Governing equations for 2D fluid

The governing equations for 2D compressible fluid are the 2D Euler equation:

$$\frac{\partial \mathbf{U}}{\partial t}+\frac{\partial \mathbf{F}}{\partial x}+\frac{\partial \mathbf{G}}{\partial y}=0, \tag{2.1}$$

where $\mathbf{U}$, $\mathbf{F}$ and $\mathbf{G}$ are given as $\mathbf{U}=(\rho,\rho u,\rho v,E)^T$, $\mathbf{F}(\mathbf{U})=\big(\rho u,\rho u^2+p,\rho uv,u(E+p)\big)^T$ and $\mathbf{G}(\mathbf{U})=\big(\rho v,\rho uv,\rho v^2+p,v(E+p)\big)^T$. Here ρ is the flow density, p is the pressure, u and v are the flow velocities in the x- and y-directions and E is the total energy which is given as $E=\rho e+0.5(\rho u^2+\rho v^2)$, where e is the specific internal energy.

A general equation of state (EOS) can be used to close the system (2.1), like $e=e(p,\rho)$ [17]. Without loss of generality, for compressible gas flows, the EOS is the perfect gas law and is given as $E=\frac{P}{\gamma-1}+\frac{1}{2}\rho(u^2+v^2)$ where γ is the specific heat ratio and is set equal to 1.4 for air. In the case of water, the Tait's equation $p=B\big(\frac{\rho}{\rho_0}\big)^N-B+A$ is utilized as the EOS. Here p_0 and ρ_0 are the reference pressure and density and equal to be $10^5 Pa$ and $1000kg/m^3$, respectively. B, A and N are constants and are set equal to $3.31\times10^8 Pa$, $1.0\times10^5 Pa$ and 7.15, respectively. The total energy of water is given as $E=\frac{P+N(B-A)}{N-1}+\frac{1}{2}\rho(u^2+v^2)$.The sound speed can be written in a unified form $c=\sqrt{\gamma}\frac{p+(B-A)}{\rho}$ where $(B-A)$ is set to 0.0 for gas.

2.1.2 Governing equations for 2D solid

The basic governing equations to be solved for elastic-plastic solids under plane strain can be written as [16]:

$$\frac{\partial \mathbf{U}}{\partial t}=\mathbf{A}\frac{\partial \mathbf{U}}{\partial x'}+\mathbf{B}\frac{\partial \mathbf{U}}{\partial y'}, \tag{2.2}$$

where

$$\mathbf{U}=\begin{bmatrix} u\\ v\\ \sigma_x\\ \sigma_y\\ \sigma_z\\ \sigma_{xy}\end{bmatrix},\quad \mathbf{A}=\begin{bmatrix} 0 & 0 & 1/\rho & 0 & 0 & 0\\ 0 & 0 & 0 & 0 & 0 & 1/\rho\\ K+4\mu/[3(1+h)] & 0 & 0 & 0 & 0 & 0\\ K-2\mu/[3(1+h)] & 0 & 0 & 0 & 0 & 0\\ K-2\mu/[3(1+h)] & 0 & 0 & 0 & 0 & 0\\ 0 & \mu/(1+h) & 0 & 0 & 0 & 0\end{bmatrix},$$

https://doi.org/10.4208/cicp.OA-2016-0212 Published online by Cambridge University Press

$$\mathbf{B}=\begin{bmatrix} 0 & 0 & 0 & 0 & 0 & 1/\rho \\ 0 & 0 & 0 & 1/\rho & 0 & 0 \\ 0 & K-2\mu/[3(1+h)] & 0 & 0 & 0 & 0 \\ 0 & K+4\mu/[3(1+h)] & 0 & 0 & 0 & 0 \\ 0 & K-2\mu/[3(1+h)] & 0 & 0 & 0 & 0 \\ \mu/(1+h) & 0 & 0 & 0 & 0 & 0 \end{bmatrix}.$$

In the above equations, K is the bulk modulus, u and v are the particle velocity along x- and y-directions, respectively, σ_x, σ_y, σ_z, σ_{xy} are stress components, ρ is the mass density, μ is the elastic shear modulus, h is the plastic factor, $\mu_p=\frac{\mu}{h+1}$ is the plastic shear modulus and it is a constant for linearly plasticity which is adopted in this paper.

2.2 Cavitation model

The cavitation may occur when the pressure in liquid water reaches towards the limit of vapor pressure. Since the cavitation model is not intended in our work, the Cutoff model [18], which is easily implemented, is adopted in this paper. The Cutoff model is a pure phase model assuming that cavitation occurs when the local pressure reaches or goes below a predefined cutoff pressure (saturated vapor pressure). With Tait's equation employed for water, the Cutoff model can be expressed as:

$$p=\begin{cases} B\left(\frac{\rho}{\rho_0}\right)^N-B+A, & \rho>\rho_{sat}, \\ p_{sat}, & \rho\leq\rho_{sat}. \end{cases} \tag{2.3}$$

Here, ρ_{sat} is the water density corresponding to the given critical pressure p_{sat}.

2.3 Elastic-plastic loading path

Here, we briefly conclude the fundamental theory of plasticity which will be used. The more details can be found in [19]. Considering an isotropic work-hardening material, which obeys von Mises' flow theory of plasticity, for the plane strain problem, the von Mises yield condition can be written as $\frac{1}{3}[(\sigma_x-\sigma_z)^2+(\sigma_y-\sigma_z)^2-(\sigma_x-\sigma_z)(\sigma_y-\sigma_z)]+(\sigma_{xy})^2=\kappa^2$, where κ is the yield stress. The elastic-plastic stress loading path in the $(\sigma_x-\sigma_z,\sigma_y-\sigma_z,\sigma_{xy})$ space, when $\sigma_y=\sigma_z$, is shown in Fig. 1. If $(\hat{\sigma}_x-\hat{\sigma}_z,\hat{\sigma}_y-\hat{\sigma}_z,\hat{\sigma}_{xy})$ is a point outside the yield surface, then point * will be the crossing point of the actual yield surface and the straight line which connects point $(\hat{\sigma}_x-\hat{\sigma}_z,\hat{\sigma}_y-\hat{\sigma}_z,\hat{\sigma}_{xy})$ with the origin.

As an example, point i is assumed to be the initial state, which is inside the initial yield surface parameterized by the value κ^*. After loading, the final state is point $(\hat{\sigma}_x-\hat{\sigma}_z,\hat{\sigma}_y-\hat{\sigma}_z,\hat{\sigma}_{xy})$ which is outside of the κ^* surface. The elastic-plastic loading path used in this paper is $(\sigma_x-\sigma_z,\sigma_y-\sigma_z,\sigma_{xy})^i\xrightarrow{\mu}(\sigma_x-\sigma_z,\sigma_y-\sigma_z,\sigma_{xy})^*\xrightarrow{\mu_p}(\hat{\sigma}_x-\hat{\sigma}_z,\hat{\sigma}_y-\hat{\sigma}_z,\hat{\sigma}_{xy})$.

https://doi.org/10.4208/cicp.OA-2016-0212 Published online by Cambridge University Press

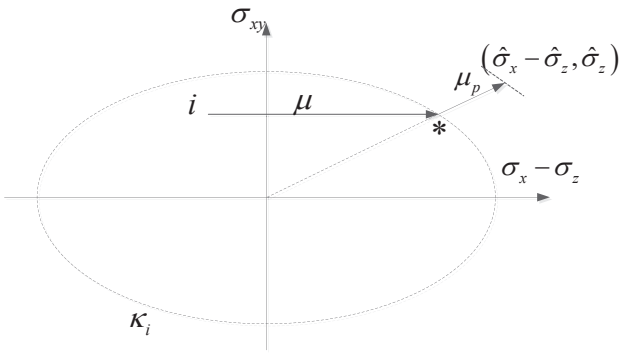


Figure 1: The sketches of the elastic-plastic stress loading path in the $(\sigma_x-\sigma_z,\sigma_y-\sigma_z,\sigma_{xy})$ space.

2.4 2D MGM-based algorithm

In this subsection, we propose a consistent, coherent approach to deal with fluid-fluid interaction, FSI and solid-solid interaction at the corresponding interfaces. For MGM-based algorithm, the Riemann problem at the interface should be firstly defined and then the solution of the Riemann problem will be used to define the ghost nodes status. After that, several single medium fields with their respective ghost field are obtained which will be solved individually. Subsequently, we advance the level set function (described in Subsection 2.5) from which the real and ghost field for each medium can be determined. Finally, we can advance the whole field from the solution of each filed based on the level set function. We will discuss each of the above steps in detail.

2.4.1 Definition of the Riemann problems at the interfaces

Here, the discussion is for the fluid-fluid, fluid-solid, solid-solid interactions at the corresponding interfaces. The definition of the Riemann problem is shown in Fig. 2. Assuming the solid line is the interface, we define the Riemann problem at every node which is at the one side of the interface, either left side or right side, and just bordering the interface. Considering node A (Fig. 2) next to the interface, we seek nodes B and C just on the other side of the interface such that they are closest to the normal η emanating from node A and on either side of the normal η. Then the variable values at nodes B and C are interpolated to get the variable value on the opposite side of the node A and on the normal η, denoted as $\mathbf{U}_{A'}$, according to the distances of B and C from η. Thus, fluid-fluid Riemann problem, fluid-solid Riemann problem and solid-solid Riemann problem along the normal direction to the interface can be defined with initial left variable value $\mathbf{U}_A$ and right variable value $\mathbf{U}_{A'}$.

2.4.2 The solution of the Riemann problems at the interfaces

The slip and non-slip conditions are employed, respectively, at the fluid-solid and solid-solid interface. For the non-slip condition employed at the solid-solid interface, the tan-

https://doi.org/10.4208/cicp.OA-2016-0212 Published online by Cambridge University Press

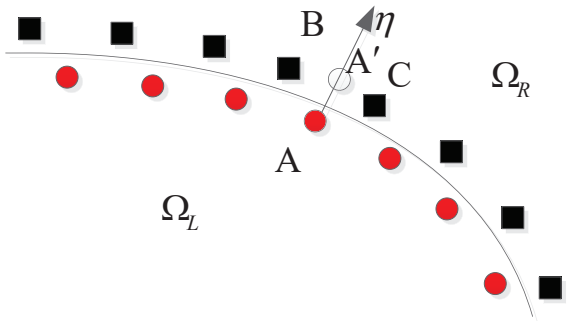


Figure 2: Schematics of the definition of Riemann problem using real nodes on both sides of the interface.

gential velocity will be continuous across the interface and the tangential component of the traction can be non-zero and equal for both solids. Since the solution of fluid-fluid Riemann problem and solid-solid Riemann problem can be found in [12, 13, 15, 16], here, the solution of fluid-solid Riemann problem is only discussed. Once $\mathbf{U}_A$ and $\mathbf{U}_{A'}$ are determined, we shall define the following Riemann problem in the perpendicular direction to the interface,

$$\begin{cases} \dfrac{\partial \mathbf{U}}{\partial t}+\dfrac{\partial F(\mathbf{U})}{\partial \eta}=\dfrac{\partial \mathbf{U}}{\partial t}+A\dfrac{\partial \mathbf{U}}{\partial \eta}=0, & \mathbf{U}(\eta,t=t^n)=\mathbf{U}_A \quad \text{for fluid,} \\ \dfrac{\partial \mathbf{U}'}{\partial t}-\dfrac{\partial \mathbf{F}'(\mathbf{U}')}{\partial \eta}=\dfrac{\partial \mathbf{U}'}{\partial t}-\mathbf{A}'\dfrac{\partial \mathbf{U}'}{\partial \eta}=0, & \mathbf{U}'(\eta,t=t^n)=\mathbf{U}'_A \quad \text{for solid.} \end{cases} \tag{2.4}$$

Here and bellow, $\eta-\xi$ represents the normal-tangential frame. For the fluid side, $\mathbf{U}=(\rho,\rho u,\rho v,E)^T$, $\mathbf{F}(\mathbf{U})=\left(\rho u,\rho u^2+p,\rho uv,u(E+p)\right)^T$, characteristic analysis leads to

$$\frac{\partial \mathbf{w}}{\partial t}+\mathbf{\Lambda}\frac{\partial \mathbf{w}}{\partial \eta}=0, \tag{2.5}$$

Here, $\mathbf{\Lambda}$ is the matrix of eigenvalues of $\mathbf{A}$, $\mathbf{w}$ is the vector of characteristic variables. For the solid side,

$$\mathbf{U}'=\begin{bmatrix} u \\ v \\ \sigma_{\eta\eta} \\ \sigma_{\xi\xi} \\ \sigma_{rr} \\ \sigma_{\xi\eta} \end{bmatrix}, \quad \mathbf{A}'=\begin{bmatrix} 0 & 0 & 1/\rho & 0 & 0 & 0 \\ 0 & 0 & 0 & 0 & 0 & 1/\rho \\ K+4\mu/[3(1+h)] & 0 & 0 & 0 & 0 & 0 \\ K-2\mu/[3(1+h)] & 0 & 0 & 0 & 0 & 0 \\ K-2\mu/[3(1+h)] & 0 & 0 & 0 & 0 & 0 \\ 0 & \mu/(1+h) & 0 & 0 & 0 & 0 \end{bmatrix}.$$

Characteristic analysis leads to

$$\frac{\partial \mathbf{w}'}{\partial t}-\mathbf{\Lambda}'\frac{\partial \mathbf{w}'}{\partial \eta}=0. \tag{2.6}$$

https://doi.org/10.4208/cicp.OA-2016-0212 Published online by Cambridge University Press

Here, $\mathbf{\Lambda}'$ is the matrix of eigenvalues of $\mathbf{A}'$ which is

$$\mathbf{\Lambda}'=\begin{bmatrix}0&0&0&0&0&0\\0&0&0&0&0&0\\0&0&\sqrt{\mu_p/\rho}&0&0&0\\0&0&0&-\sqrt{\mu_p/\rho}&0&0\\0&0&0&0&\sqrt{\frac{3K+4\mu_p}{3\rho}}&0\\0&0&0&0&0&-\sqrt{\frac{3K+4\mu_p}{3\rho}}\end{bmatrix}.$$

$\mathbf{w}'$ is the vector of characteristic variables which comes from $\mathbf{w}'=\mathbf{S}'\mathbf{U}'$, where $\mathbf{S}'$ is the left eigen matrix of $\mathbf{A}'$:

$$\mathbf{S}'=\begin{bmatrix}0&0&(2\mu_p-3K)/(4\mu_p+3K)&0&1&0\\0&0&(2\mu_p-3K)/(4\mu_p+3K)&1&0&0\\0&0&\sqrt{\rho\mu_p/2}&0&0&1/2\\0&0&-\sqrt{\rho\mu_p/2}&0&0&1/2\\\frac{(3K-2\mu_p)\sqrt{\rho}}{2\sqrt{9K+12\mu_p}}&0&\frac{(3K-2\mu_p)}{2(4\mu_p+3K)}&0&0&0\\\frac{(-3K+2\mu_p)\sqrt{\rho}}{2\sqrt{9K+12\mu_p}}&0&\frac{(3K-2\mu_p)}{2(4\mu_p+3K)}&0&0&0\end{bmatrix}.$$

$\mathbf{w}'$ is calculated as

$$\mathbf{w}'=\mathbf{S}'\mathbf{U}'=\begin{bmatrix}\sigma_{\eta\eta}\frac{(2\mu_p-3K)}{(4\mu_p+3K)}+\sigma_{rr}\\\sigma_{\eta\eta}\frac{(2\mu_p-3K)}{(4\mu_p+3K)}+\sigma_{\xi\xi}\\\mu_\xi\frac{\sqrt{\rho\mu_p}}{2}+\frac{\sigma_{\xi\eta}}{2}\\-\mu_\xi\frac{\sqrt{\rho\mu_p}}{2}+\frac{\sigma_{\xi\eta}}{2}\\\frac{(3K-2\mu_p)\sqrt{\rho}}{2\sqrt{9K+12\mu_p}}\mu_\eta+\frac{(3K-2\mu_p)}{2(4\mu_p+3K)}\sigma_{\eta\eta}\\-\frac{(3K-2\mu_p)\sqrt{\rho}}{2\sqrt{9K+12\mu_p}}\mu_\eta+\frac{(3K-2\mu_p)}{2(4\mu_p+3K)}\sigma_{\eta\eta}\end{bmatrix}.$$

Like what was done for fluid-fluid and solid-solid Riemann problem [12, 13, 15, 16], here we solve the fluid-solid Riemann problem by characteristic analysis of Eq. (2.4). Fig. 3 shows the characteristic method used to solve the fluid-solid Riemann problem with assumption of that fluid and solid are on the left and right side of the interface, respectively. In the following, the subscripts, I, IL and IR are used to indicate if an interfacial value is calculated on the interface, left and right side of the interface. The other nomenclature is consistent with the preceding parts.

The characteristic of left side of (2.4) corresponding to the eigenvalue $u+c$ (C^+ in Fig. 3) is

$$\frac{du}{dt}+\frac{1}{\rho c}\frac{dp}{dt}=0. \tag{2.7}$$

https://doi.org/10.4208/cicp.OA-2016-0212 Published online by Cambridge University Press

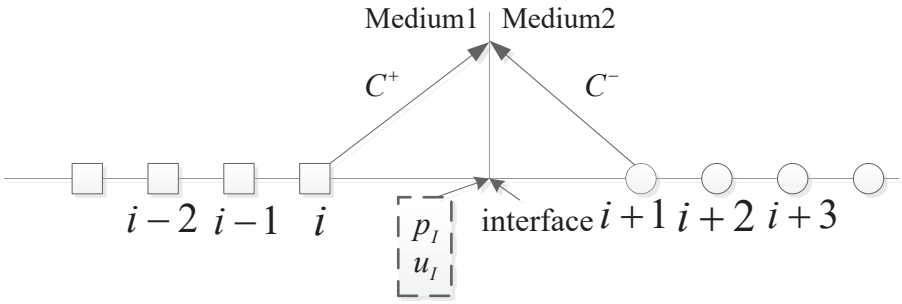


Figure 3: The characteristics used to solve the fluid-solid Riemann problem (Note that the spatial extent between nodes i and $i+1$ is exaggerated for better illustration.

The characteristics of right side of (2.4) corresponding to the eigenvalue $\sqrt{\frac{3K+4\mu_p}{3\rho}}$ (C^- in Fig. 3) is

$$\frac{d\left(\frac{(3K-2\mu_p)\sqrt{\rho}}{\sqrt{9K+12\mu_p}}\mu_p+\frac{3K-2\mu_p}{4\mu_p+3K}\sigma_{\eta\eta}\right)}{dt}=0. \tag{2.8}$$

By integrating the characteristics of Eq. (2.7), we can obtain $(u_\eta)_I=(u_\eta)_i+\int_{p_i}^{p_I}\frac{dp}{\rho c}$ which is approximated by

$$p_I=p_i-\rho_i c_i\left((u_\eta)_I-(u_\eta)_i\right)=p_i-W_L\left((u_\eta)_I-(u_\eta)_i\right). \tag{2.9a}$$

where $W_L=\rho_i c_i$. Integrating the characteristic of Eq. (2.8) gives rise to

$$\int_R^{IR} d\left(\frac{(3K-2\mu_p)\sqrt{\rho}}{\sqrt{9K+12\mu_p}}u_\eta\right)=-\int_R^{IR} d\left(\frac{(3K-2\mu_p)}{4\mu_p+3K}\sigma_{\eta\eta}\right). \tag{2.9b}$$

Assuming the solid undergoes elastic deformation, with the constant $\mu_p=\mu$, the integral in Eq. (2.9b) has a closed form, which gives rise to

$$\left(\frac{(3K-2\mu)\sqrt{\rho}}{2\sqrt{9K+12\mu}}u_\eta+\frac{3K-2\mu}{2(4\mu+3K)}\sigma_{\eta\eta}\right)_I=\left(\frac{(3K-2\mu)\sqrt{\rho}}{2\sqrt{9K+12\mu}}u_\eta+\frac{3K-2\mu}{2(4\mu+3K)}\sigma_{\eta\eta}\right)_{i+1}.$$

For ease of reference, it can be rewritten as

$$(A\mu_\eta+B\sigma_{\eta\eta})_I=(A\mu_\eta+B\sigma_{\eta\eta})_{i+1}. \tag{2.10}$$

where $A=\frac{(3K-2\mu)\sqrt{\rho}}{2\sqrt{9K+12\mu}}$, $B=\frac{(3K-2\mu)}{2(4\mu+3K)}$. With balance of force, we have $p_I=-(\sigma_{\eta\eta})_I$. Thus, the system (2.9) can be solved to obtain the interfacial pressure (normal stress for solid) and normal velocity as follows:

$$p=\begin{cases}\left(\frac{A}{W_L}+B\right)(\sigma_{\eta\eta})_I=\left(-\frac{A}{W_L}p_i-A(u_\eta)_i+A(u_\eta)_{i+1}+B(\sigma_{\eta\eta})_{i+1}\right),\\ \left(\frac{A}{W_L}+B\right)(u_\eta)_I=\frac{B}{W_L}p_i+B(u_\eta)_i+\frac{A}{W_L}(u_\eta)_{i+1}+\frac{B}{W_L}(\sigma_{\eta\eta})_{i+1}.\end{cases} \tag{2.11}$$

https://doi.org/10.4208/cicp.OA-2016-0212 Published online by Cambridge University Press

The tangential velocity and shear stress at the interface are copied from the local real nodes. Integrating the two characteristics of right side of (2.4) corresponding to the zero eigenvalue, we can derive $\sigma_{\xi\xi I}$ and σ_{rrI} as $\sigma_{\xi\xi I}=(\sigma_{\eta\eta}B+\sigma_{\xi\xi})_R-B\sigma_{\eta\eta I}$ and $\sigma_{rrI}=(A\sigma_{\eta\eta}+\sigma_{rr})_R-A\sigma_{\eta\eta I}$, respectively. The fluid density at the interface is provided by the Tait EOS in the case of water or the energy jump condition [12]. This way, we can determine all the interfacial variables ($\mathbf{U}_{IL}=(p_I,(u_\mu)_I,(u_\xi)_I,\rho_{IL})^T$, for the ghost fluid and $\mathbf{U}_{IR}=((\sigma_{\eta\eta})_I,(u_\mu)_I,(\sigma_{\xi\xi})_I,(u_\xi)_I,(\sigma_{\xi\eta})_I)^T$ for the ghost solid) to define the states of the ghost nodes.

The above process is under the assumption that the solid undergoes elastic deformation. The cases in which the solid undergoes plastic deformation and the cavitation occurs in water are discussed below.

For solid undergoing plastic deformation, namely $\frac{1}{3}\left[(\sigma_x-\sigma_z)^2+(\sigma_y-\sigma_z)^2-(\sigma_x-\sigma_z)(\sigma_y-\sigma_z)\right]+\left(\sigma_{xy}\right)^2>\kappa^2$, according to the loading path proposed in Subsection 2.3 (see Fig. 1), firstly we determine the point * in Fig. 1 by

$$
\begin{aligned}
(\sigma^*_{\eta\eta}-\sigma^*_{rr})_{IR}&=\frac{(\hat{\sigma}_{\eta\eta}-\hat{\sigma}_{rr})_{IR}}{\hat{\kappa}_{IR}}\kappa^*_{IR},\\
(\sigma^*_{\xi\xi}-\sigma^*_{rr})_{IR}&=\frac{(\hat{\sigma}_{\xi\xi}-\hat{\sigma}_{rr})_{IR}}{\hat{\kappa}_{IR}}\kappa^*_{IR},\\
(\sigma^*_{\xi\eta})_{IR}&=\frac{(\hat{\sigma}_{\xi\eta})_{IR}}{\hat{\kappa}_{IR}}\kappa^*_{IR}
\end{aligned}
$$

and we choose $(u_\eta)^*_I$ and $(u_\xi)^*_I$ from the solution under elastic deformation assumption. This is because the velocities (u_η) and (u_ξ) are calculated by solving the continuity equations and only depend on the density, it is not required to calculate the equivalent *-values for them. Thus, the loading path is determined as

$$
(\sigma_{\eta\eta}-\sigma_{rr},\sigma_{\xi\xi}-\sigma_{rr},\sigma_{\xi\eta})\xrightarrow{\mu}(\sigma^*_{\eta\eta}-\sigma^*_{rr},\sigma^*_{\xi\xi}-\sigma^*_{rr},\sigma^*_{\xi\eta})\xrightarrow{\mu_p}(\hat{\sigma}_{\eta\eta}-\hat{\sigma}_{rr},\hat{\sigma}_{\xi\xi}-\hat{\sigma}_{rr},\hat{\sigma}_{\xi\eta}).
$$

Then the integration of Eq. (2.9b) leads to

$$
A_p(u_\eta)_I+A(u_\eta)^*_I-A(u_\eta)_{i+1}-A_p(u_\eta)^*_I=-\left(B_p(\sigma_{\eta\eta})_I+B(\sigma_{\eta\eta})^*_I-B(\sigma_{\eta\eta})_{i+1}-B_p(\sigma_{\eta\eta})^*_I\right). \tag{2.12}
$$

where $A_p=\frac{(3K-2\mu_p)\sqrt{\rho}}{2\sqrt{9K+12\mu_P}}$, $B_p=\frac{(3K-2\mu_p)}{2(4\mu_p+3K)}$, A and B are the same as that in Eq. (2.10). From Eqs. (2.9a) and (2.12), with $p_I=-(\sigma_{\eta\eta})_I$, the interfacial pressure and normal velocity are given by

$$
\begin{aligned}
\left(\frac{A_p}{W_L}-B_p\right)(\sigma_{\eta\eta})_I=&-\frac{A_p}{W_L}p_i+B_p(\sigma_{\eta\eta})^*_I+B\left((\sigma_{\eta\eta})^*_I-(\sigma_{\eta\eta})_{i+1}\right)\\
&-A_p\left((u_\eta)_i-(u_\eta)^*_I\right)-A\left((u_\eta)^*_I-(u_\eta)_{i+1}\right)
\end{aligned}
$$

https://doi.org/10.4208/cicp.OA-2016-0212 Published online by Cambridge University Press

and

$$(A_p+1)(u_\eta)_I=\left(\frac{1}{W_L}-B_p\right)(\sigma_{\eta\eta})_I+\frac{1}{W_L}p_i+B_p(\sigma_{\eta\eta})_I^*-B\left((\sigma_{\eta\eta})_I^*-(\sigma_{\eta\eta})_{i+1}\right)$$
$$+A\left((u_\eta)_{i+1}-(u_\eta)_I^*\right)+A_p(u_\eta)_I^*+(u_\eta)_i,$$

respectively. The tangential velocity and shear stress at the interface are copied from the local real nodes. Integrating the two characteristics of right side of (2.4) corresponding to the zero eigenvalue, the $\sigma_{\xi\xi I}$ and σ_{rrI} can be derived as $(\sigma_{\xi\xi})_I=(\sigma_{\xi\xi})_{i+1}+2B_p(\sigma_{\eta\eta})_I+2B(\sigma_{\eta\eta})_I^*-2B(\sigma_{\eta\eta})_{i+1}+2B_p(\sigma_{\eta\eta})_I^*$ and $(\sigma_{rr})_I=(\sigma_{rr})_{i+1}+2B_p(\sigma_{\eta\eta})_I+2B(\sigma_{\eta\eta})_I^*-2B(\sigma_{\eta\eta})_{i+1}+2B_p(\sigma_{\eta\eta})_I^*$, respectively. Thus, we can determine all the interfacial variables ($\mathbf{U}_{IL}=(p_I,(u_\mu)_I,(u_\xi)_I,\rho_{IL})^T$ for the ghost fluid and $\mathbf{U}_{IR}=((\sigma_{\eta\eta})_I,(u_\mu)_I,(\sigma_{\xi\xi})_I,(u_\xi)_I,(\sigma_{\xi\eta})_I)^T$ for the ghost solid) to define the states of the ghost nodes with solid undergoing plastic deformation. In practice, alternatively, we can treat the solid undergoing plastic deformation with the same way for the solid undergoing elastic deformation by simply replacing A with A_p and B with B_p and the result turns out to be the same. For the case that cavitation occurs in fluid, we assign the interfacial pressure equal to the vapor pressure and the interfacial normal velocity equal to the solid velocity. The other variables are derived in the same way as above.

2.4.3 Defining the states on ghost fluid and solid nodes

The way discussed here is used to define the states on ghost fluid and solid nodes corresponding to all the three kinds of interfaces (fluid-fluid interface, fluid-solid interface and solid-solid interface). For any ghost node (take the node G in Fig. 4 as an example), firstly, we search for the nearest real node bordering the interface and on the opposite side of the interface. Then we choose the other bordering real node next to the selected node such that the ghost node is between the two lines (η_1 and η_2 in Fig. 4) emanating from the two selected bordering nodes along the normal directions. Then the variable value and the material properties on the ghost node G can be determined by the interpolation of the interfacial status on the opposite side of ghost node G, which is solved at

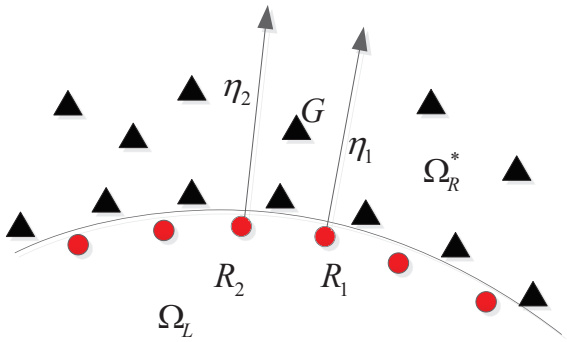


Figure 4: Schematics of how to define the status over the ghost node G.

https://doi.org/10.4208/cicp.OA-2016-0212 Published online by Cambridge University Press

the two selected bordering nodes (R_1 and R_2 in Fig. 4) using the interfacial variables discussed in Section 2.4.2, according to the distances from the two lines (η_1 and η_1 in Fig. 4). After extrapolation, the resulting variables need to be transformed back to original $x-y$ coordinate system.

After the states on all the ghost nodes are determined, we get several single-medium problems corresponding to the media involved with ghost nodes. They can be solved with desirable numerical solvers and the solution of each medium will be used to update the whole real field based on the interface location.

2.5 Capturing the evolution of the interface

MGM employs level set technique together with re-initialization to implicitly capture the fluid-fluid and fluid-solid interfaces. Like what was done in [11,13], the extension velocity is used to advance the level set function. Since the level set technique has been widely used in previous work [20,21], the details about the level set technique are neglected here.

2.6 Lagrangian mesh for solid

Since the solid mesh is of updated Lagrangian type, i.e., the real solid nodes will move with the local material velocity (u_{new} and v_{new} in Eqs. (2.13) and (2.14)), the new positions of the real solid nodes are updated at every time-step according to:

$$X_{new} = X_{old} + \Delta X, \Delta X = u_{new}\Delta t; \tag{2.13}$$

$$Y_{new} = Y_{old} + \Delta Y, \Delta Y = v_{new}\Delta t. \tag{2.14}$$

The new positions of the ghost solid nodes are updated in the same way with the real solid nodes, except with the velocities of the real solid nodes closest to the targeted nodes and immediately nearest to the interface. Similar approaches can be found in [22,23].

3 Numerical experiments

In this section, for ease of reference, subscripts g, w, and s represent gas, water, and solid, respectively. Two kinds of solids are adopted; one is the stainless steel AISI 431 [24] with Poisson ration 0.283, Young's modulus $215.116Gpa$ and density $7.7kg/m^3$ and the other one is a (physically nonexistent) material with only the Young's modulus changed to $315.116Gpa$ based on AISI 431. Both the elastic limits for the two solid materials are set as $850MPa$. The plastic shear modulus is set as $\mu_p = 0.8\mu$. In the following, solid1 and solid2 are used to represent the AISI 431 and the other solid material, respectively. All the variables in the calculations are nondimensionalized with the following reference

https://doi.org/10.4208/cicp.OA-2016-0212 Published online by Cambridge University Press

parameters,

$$\rho_{ref}=1000kg/m^3,\quad P_{ref}=1.0\times10^5Pa,\quad L_{ref}=1.0m,$$
$$u_{ref}=\sqrt{\frac{P_{ref}}{\rho_{ref}}}=10.0m/s,\quad t_{ref}=\frac{L_{ref}}{u_{ref}}=0.1s.$$

Here, ρ_{ref}, P_{ref}, L_{ref}, u_{ref} and t_{ref} are the reference density, pressure, length, velocity and time, respectively.

Since the MGFM for fluid-fluid interaction and MGSM for solid-solid interaction have already been validated in previous work [12, 13, 15, 16], firstly, we validate the MGM for FSI. Next, we verify the validity of MGM for a 2D gas-water-solid1-solid2 interaction problem. Then, the solid structures with different configurations subjected to underwater explosion which involve all kinds of medium are numerically simulated using the MGM. For all the numerical experiments, we adopt first-order Godunov method to solve both the fluids and solids. The space interval is uniform which is 0.05 all over the field. The CFL number is set to be 0.45.

3.1 Case 1: Gas-Solid1 interaction

The solution domain is $\Omega=\{(x,y)|x\in[0,10],y\in[0,4]\}$ and the gas-solid1 interface is defined by $y=7-x$ inclining at 45° to the (horizontal) x-axis. The schematic of this case is shown in Fig. 5. All the media are static initially, i.e., the initial velocity are zero. The other initial variables are $\rho_g=0.05$, $p_g=10000.0$, $\sigma_\eta=-1.0$, $\sigma_{\bar{\xi}}=0.0$ and $\sigma_{\bar{\xi}\eta}=0.0$. The computation is allowed to run till 2.0e-3.

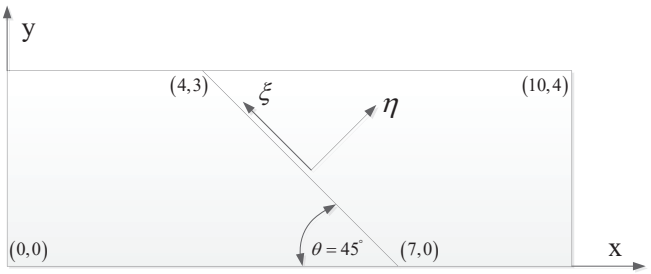
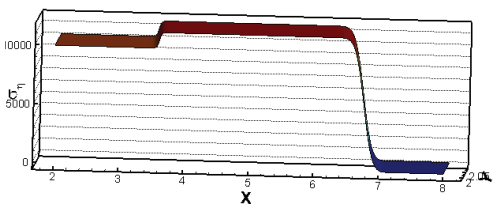


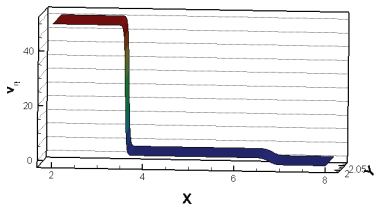
Figure 5: Schematic illustration of the Case 1.

In Fig. 6, the results are plotted for the region $\Omega=\{(x,y)|x\in[2,8],y\in[1.98,2.08]\}$ to show the region of major changes. Figs. 6(a)-(b) indicate that the pressure (or negative normal stress) and the normal velocity are continuous across the interface. Figs. 6(c)-(d) show that both the tangential velocity and shear stress suffer from very limited oscillations which are well within the bounds of the numerical error of the solver for the used discretization. Fig. 6(e) shows the tangential stress for solid are stable and smooth. The 2D results are in great agreement with the analytic equivalent 1D solution as well as the

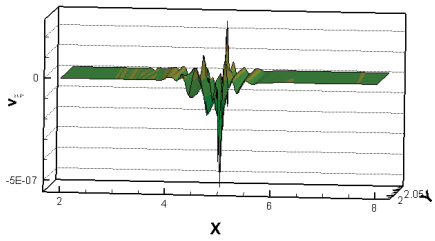
https://doi.org/10.4208/cicp.OA-2016-0212 Published online by Cambridge University Press



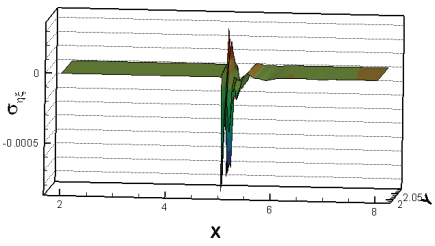
(a) pressure profile



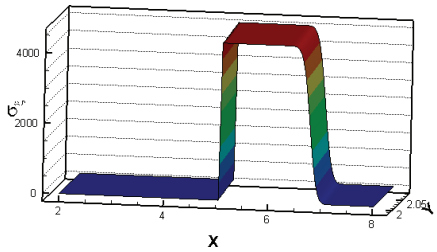
(b) normal velocity profile



(c) tangential velocity profile



(d) shear stress profile



(e) tangential stress profile

Figure 6: The numerical results for Case 1.

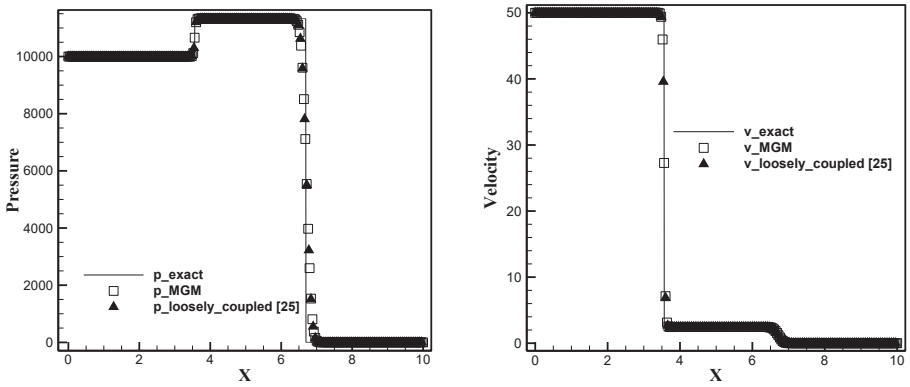


Figure 7: Normal stress and velocity with respect to the normal coordinate (η) for Case 1.

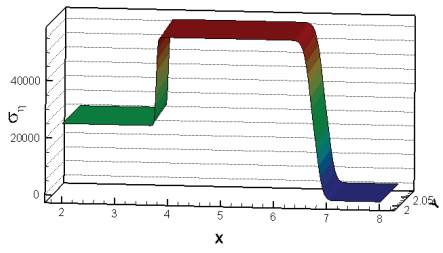
https://doi.org/10.4208/cicp.OA-2016-0212 Published online by Cambridge University Press

numerical-based loosely coupled solution [25], along the normal direction to the interface (see Fig. 7), which shows that the validity and accuracy of the present method.

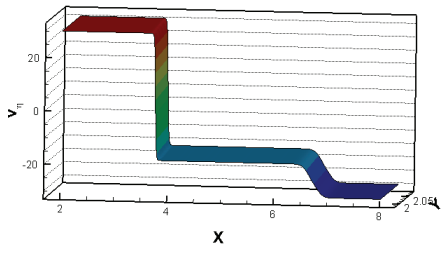
3.2 Case 2: Water-Solid1 interaction

The initial setup and coordinate system used in this case are similar to those used in Case 1. All the media are static initially, i.e., the initial velocity are zero. The other initial variables are $\rho_w = 1.0$, $p_w = 25000.0$, $\sigma_\eta = -25.0$, $\sigma_{\bar{\xi}} = 0.0$ and $\sigma_{\bar{\xi}\eta} = 0.0$. The computation is allowed to run till $2.0e-3$.

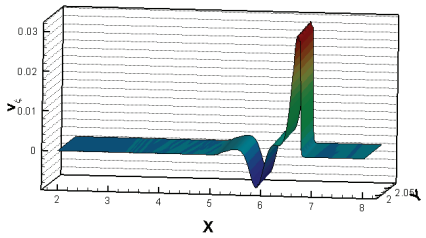
In Fig. 8, the results are plotted for the region $\Omega = \{(x,y)|x \in [2,8], y \in [1.98,2.08]\}$ to show the region of major changes for the computed variables. Similar to the case 1, the pressure (or negative normal stress) and normal velocity are smooth and continuous across the interface (see Figs. 8(a)-(b)). The tangential stress for solid is stable and smooth (see Fig. 8(e)). From Figs. 8(c)-(d), we find that the tangential velocity and shear



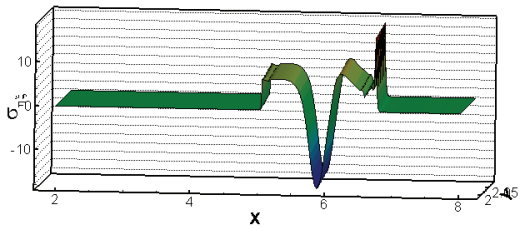
(a) pressure profile



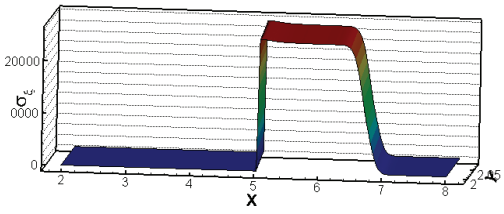
(b) normal velocity profile



(c) tangential velocity profile



(d) shear stress profile



(e) tangential stress profile

Figure 8: The numerical results for Case 2.

https://doi.org/10.4208/cicp.OA-2016-0212 Published online by Cambridge University Press

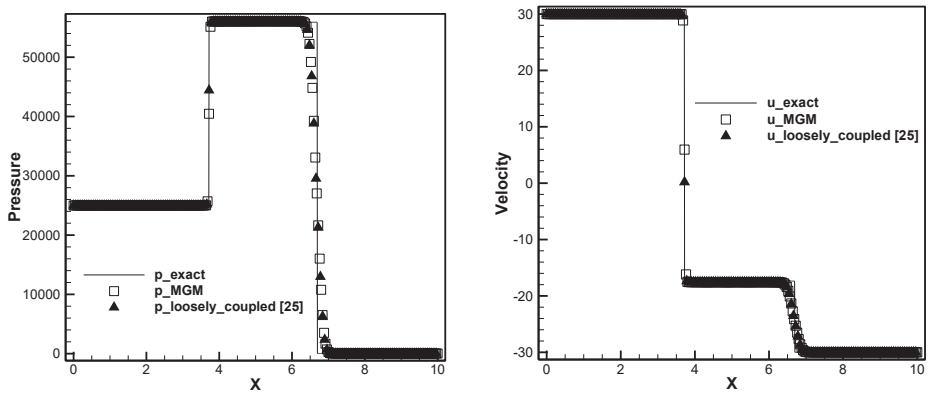


Figure 9: Normal stress and velocity with respect to the normal coordinate (η) for Case 2.

stress for solid suffer slight non-physical oscillations which are severer than that in Case 1. That is because the initial pressure in water is so high that the solid undergoes plastic deformation, which increases the accumulation of the numerical error. Even so, the non-physical oscillations are very low and negligible compared to normal velocity and pressure. The 2D solutions compare well with the analytic equivalent 1D solution as well as the numerical-based loosely coupled solution as shown in Fig. 9. It once again shows the validity and accuracy of the present method.

3.3 Case 3: Gas-Water-Solid1-Solid2 interaction

The schematic of this case is shown in Fig. 10. All the media are static initially, i.e., the initial velocity are zero. The other initial variables are $\rho_g = 1.27$, $p_g = 8270.0$, $\rho_w = 1.0$, $p_w = 1.0$, $(\sigma_\eta)_{s1,s2} = -1.0$, $(\sigma_\xi)_{s1,s2} = 0.0$ and $(\sigma_{\xi\eta})_{s1,s2} = 0.0$. The computation is allowed to run till 0.011.

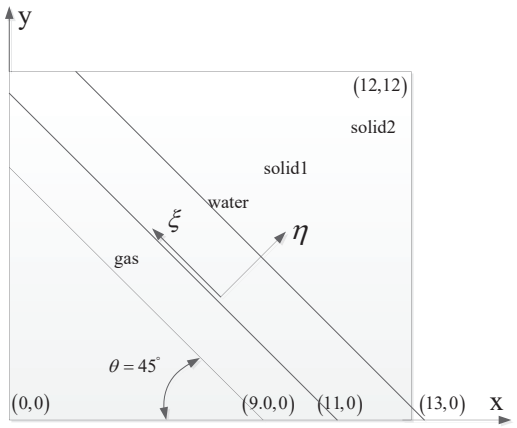
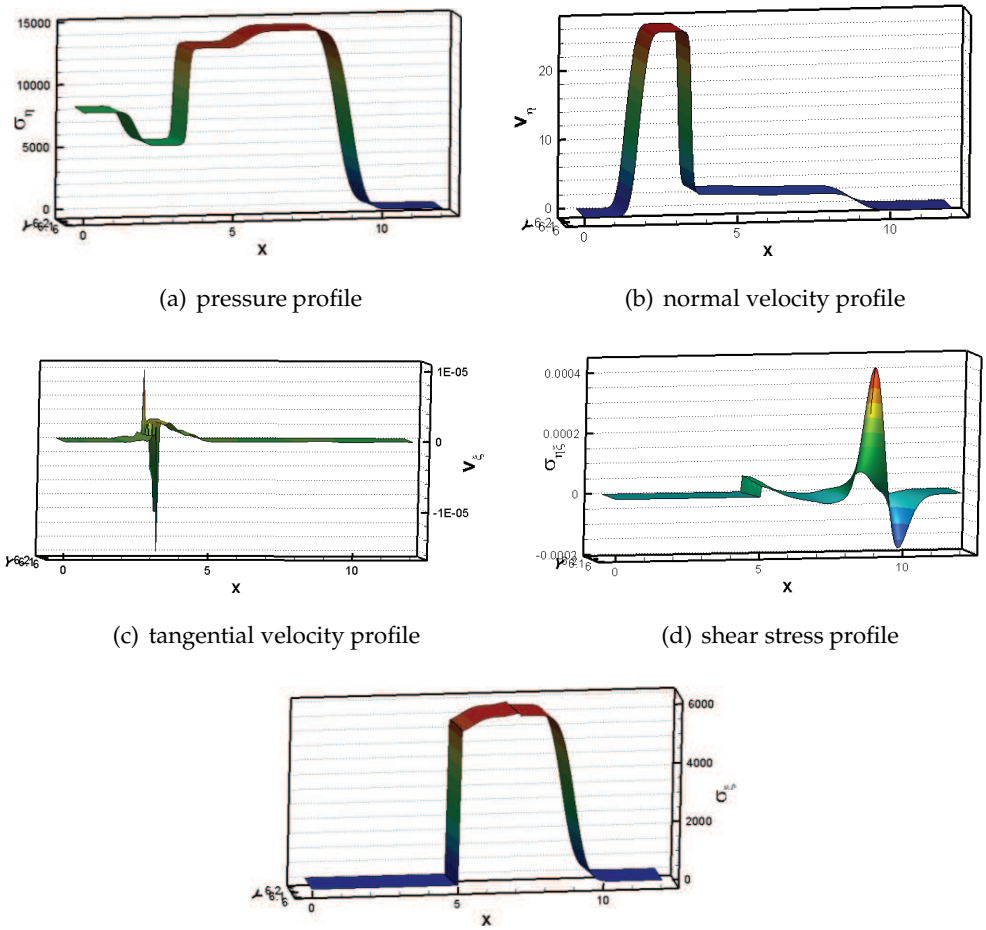


Figure 10: Schematic illustration of the Case 3.

https://doi.org/10.4208/cicp.OA-2016-0212 Published online by Cambridge University Press



(a) pressure profile

(b) normal velocity profile

(c) tangential velocity profile

(d) shear stress profile

(e) tangential stress profile

Figure 11: The numerical results for Case 3.

In Fig. 11, the results are plotted for the region $\Omega = \{(x,y)|x \in [0,12], y \in [6.1,6.2]\}$ to show the region of major changes for the computed variables. Initially, the shock front coincides with the gas-water interface. The shock wave moves towards the solid side, following by the wave refraction occurred at the water-solid interface. Then the shock continues to propagate until it impacts the solid-solid interface. Since the solid2 is 'harder' than solid1, the loading wave is reflected in solid1. The pressure (or negative normal stress) and normal velocity are smooth and continuous across the all the interfaces (see Figs. 11(a)-(b)). The tangential stress for solid is stable and smooth (see Fig. 11(e)). From Figs. 11(c)-(d), we find that the tangential velocity and shear stress for solid suffer from very limited oscillations which are well within the bounds of the numerical error of the solver for the used discretization. The 2D solutions compare well with the analytic

https://doi.org/10.4208/cicp.OA-2016-0212 Published online by Cambridge University Press

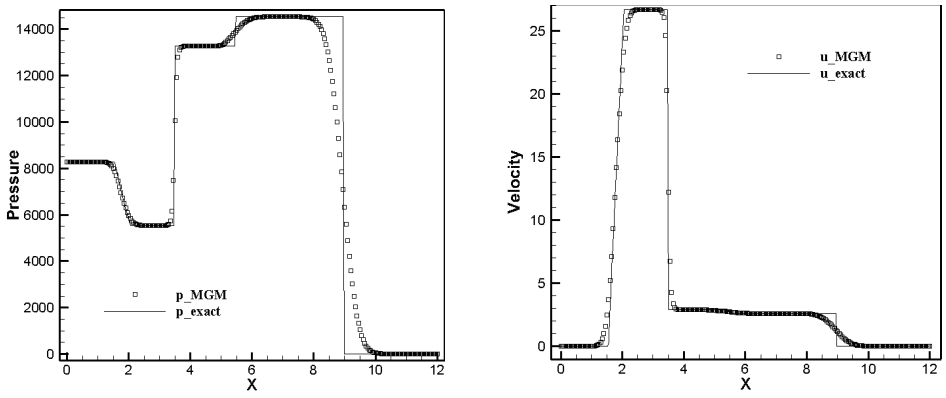


Figure 12: Normal stress and velocity with respect to the normal coordinate (η) for Case 3.

equivalent 1D solution as shown in Fig. 12. The convergence of the numerical method is carried out by mesh refinement. Fig. 13 shows the L_1-norm convergence rate for both the normal pressure and velocity with double mesh refinement and a first order error is observed that is consistent with the single medium solver employed.

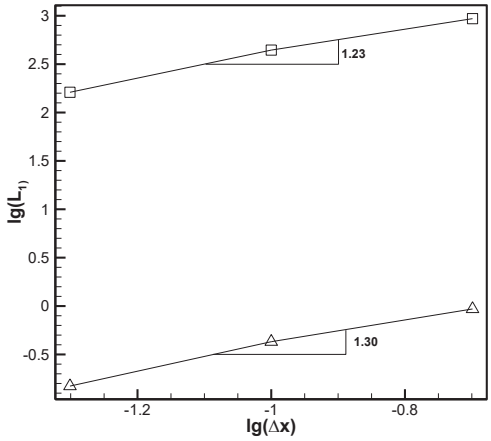


Figure 13: The mesh convergence rate for both the normal pressure and velocity for Case 3.

3.4 Case 4: The interaction between underwater explosion and solid structure

The whole domain is $\Omega=\{(x,y)|x\in[-6,6],y\in[-6,6]\}$ comprising of gas, water and solid. The underwater explosion is achieved by assuming a zone filled with ideal gas of high pressure and density initially located at the origin 0,0 with radius $1.0m$. The surrounding water is at atmospheric pressure. Pressure equilibrium is initially across the water-solid interface which is vertical line located at $x=3.025m$. Fig. 14 provides the schematic of this

https://doi.org/10.4208/cicp.OA-2016-0212 Published online by Cambridge University Press

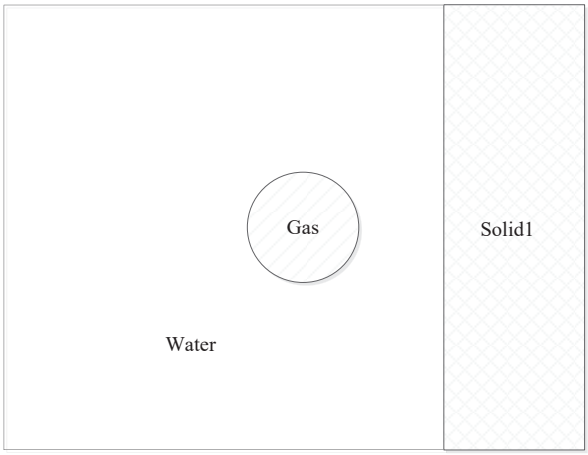
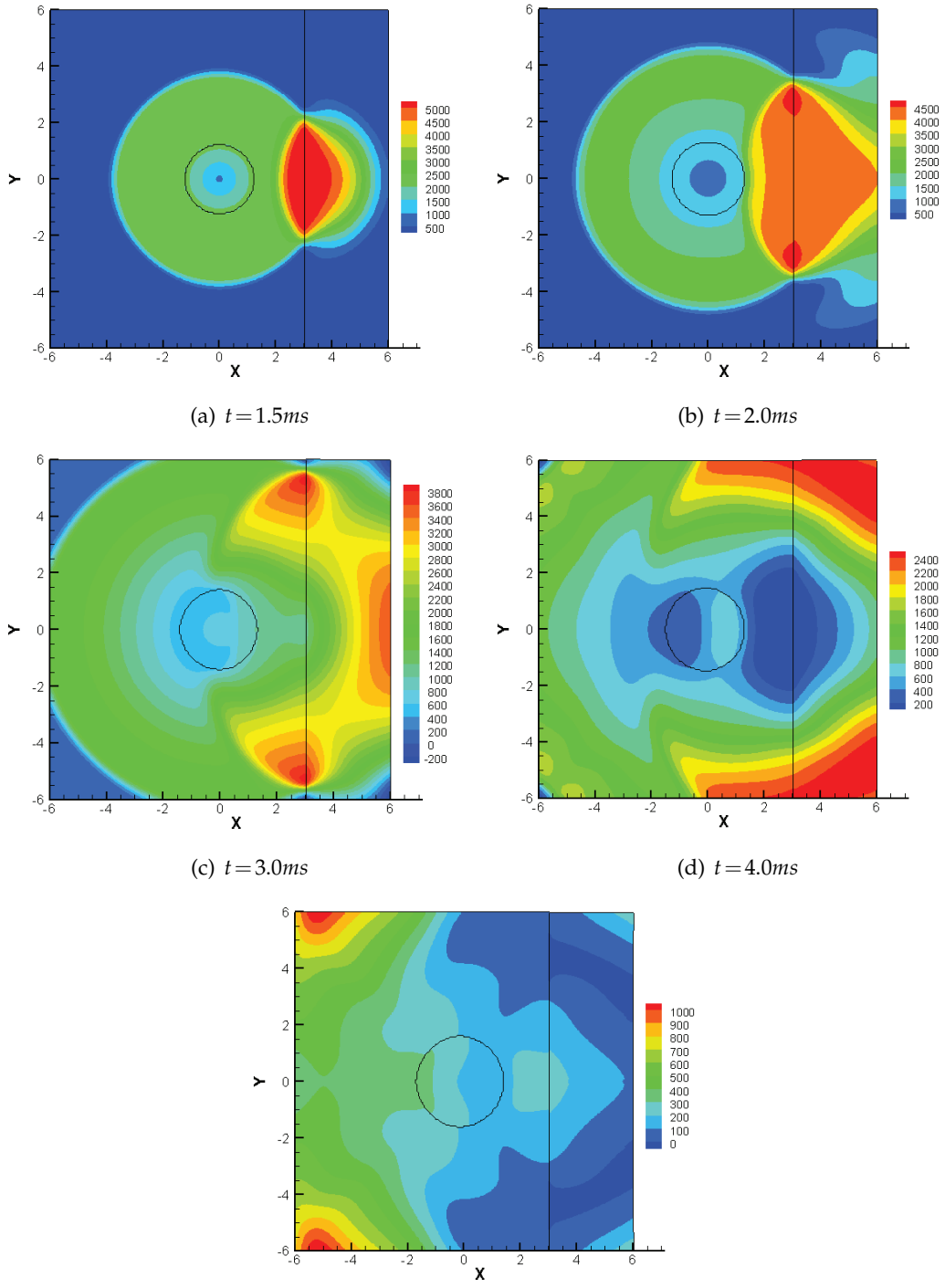


Figure 14: Schematic illustration of Case 4.

case. All the media are static initially, i.e., the initial velocity are zero. The other initial variables are $\rho_g=1.27$, $p_g=8290.0$, $\rho_w=1.0$, $p_w=1.0$, $\sigma_\eta=-1.0$, $\sigma_\xi=-0.3947$ and $\sigma_{\xi\eta}=0.0$. The computation is allowed to run till 0.065.

The pressure distributions (or negative stress along x-direction) at different significant instants are displayed in Figs. 15(a)-(e). The solid lines represent the bubble and the fluid-solid interface. The sequence of events that occur as the high pressure explosive bubble expands and pressure wave emanates from it and thereby affecting the nearby media may be described as below. Shock waves are initially generated by the explosive bubble moving outwards and when it impacts the water-solid interface, it is reflected back towards the bubble (see Fig. 15(a)). When this reflected shock wave hits the gas bubble, a reflected rarefaction wave and a transmitted shock wave are generated (see Fig. 15(b)). Fig. 15(c) shows afterwards, the reflected rarefaction wave hits the solid wall and is reflected back from the wall, which leads to the decrease of the pressure near the wall. These repetitive processes give rise to the cavitation near the wall and the growth of cavitation, as illustrated in Fig. 15(d). The cavitation region then collapses as shown in Fig. 15(e). With time, the transmitted shock wave keeps on traveling through the bubble and creates complex pattern of pressure distribution. For the solid, compressive elastic waves are generated in the solid subjected to the initial shock wave. Fig. 15(a) indicates the propagation of the elastic wave. At 3 milliseconds, the σ_{xx} component near the water-solid interface and the x-axis becomes less compressive as the pressure on the fluid side has become relatively low (Fig. 15(c)). As cavitation occurs near the fluid-solid interface, the stress σ_{xx} becomes the least compressive (Fig. 15(d)). After the collapse of the cavitation, the compressive waves that are generated reload the structure (Fig. 15(e)). Fig. 16 shows the evolution of the high pressure bubble. The bubble is found to grow and the side near the solid is suppressed. The deformation of the water-solid interfaces is very small, which is not shown.

https://doi.org/10.4208/cicp.OA-2016-0212 Published online by Cambridge University Press



(a) $t=1.5ms$ (b) $t=2.0ms$

(c) $t=3.0ms$ (d) $t=4.0ms$

(e) $t=6.5ms$

Figure 15: Pressure distribution for Case 4.

https://doi.org/10.4208/cicp.OA-2016-0212 Published online by Cambridge University Press

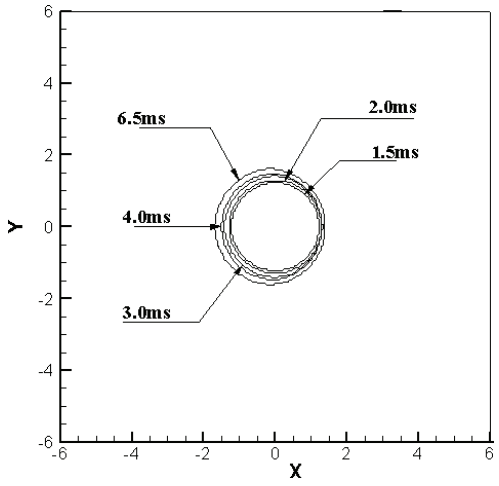


Figure 16: The evolution of the gas-water interface with respect to time for Case 4.

3.5 Case 5: The interaction between underwater explosion and complex solid structure with a circular inclusion

The whole domain is $\Omega = \{(x,y)|x \in [-6,8], y \in [-6,6]\}$ comprising of gas, water and solid. The initial setup and condition used in this case are the same as those used in Case 4, except that the circular solid2 is located at the $(4.5,0)$ with radius $1.0m$ in the solid1 (see Fig. 17). The computation is allowed to run till 0.065.

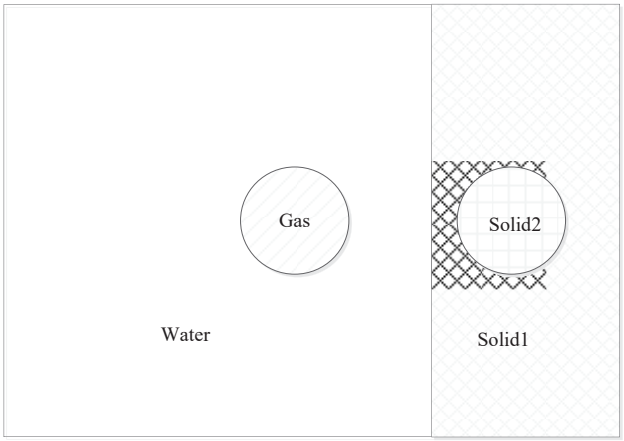
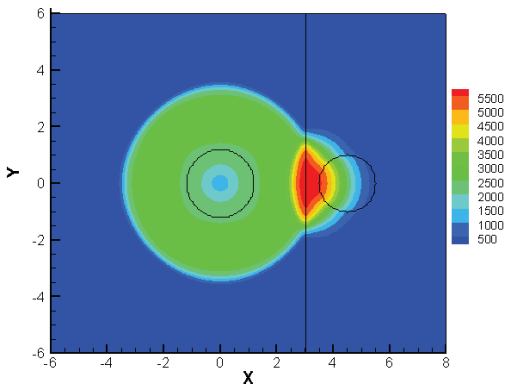


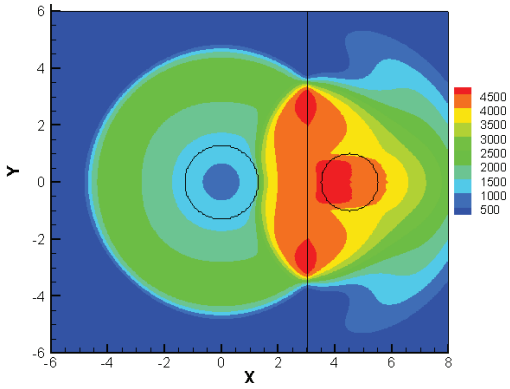
Figure 17: Schematic illustration of Case 5.

The pressure distributions (or negative stress along x-direction) at different significant instants are displayed in Figs. 18(a)-(e). The solid lines represent the bubble, the fluid-solid interface and the circular solid inclusion. The whole process of the interac-

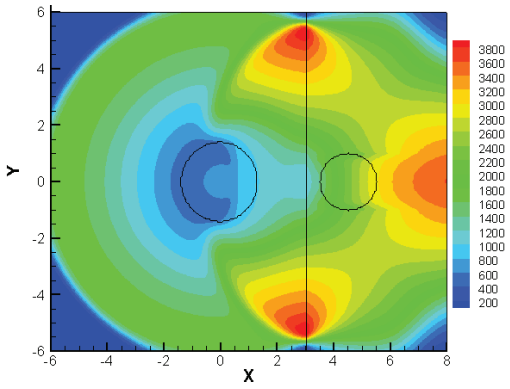
https://doi.org/10.4208/cicp.OA-2016-0212 Published online by Cambridge University Press



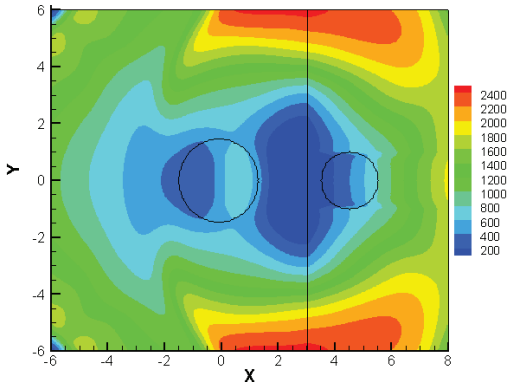
(a) $t=1.3ms$



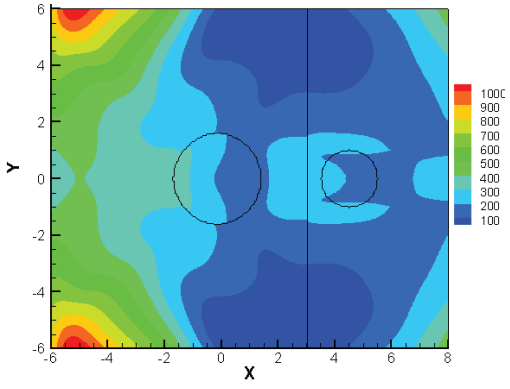
(b) $t=2.0ms$



(c) $t=3.0ms$



(d) $t=4.0ms$



(e) $t=6.5ms$

Figure 18: Pressure distribution for Case 5.

https://doi.org/10.4208/cicp.OA-2016-0212 Published online by Cambridge University Press

tion between underwater explosion and the solid structure is very similar to the Case 4. So we only describe the differences caused by the circular inclusion. Because solid2 is harder than solid1, namely the Young's modulus of solid2 is bigger than that of solid1, faster loading waves inside solid2, compared with the waves in solid1, are observed in Figs. 18(a)-(b). As a result of the circular solid inclusion in the solid structure, the response of solid structure subjected to underwater explosion in this case is changed (see Fig. 18). The deformation of the bubble is similar to that in Case 4 and not shown here. The deformation of the water-solid interface and solid-solid interface is very slightly, which is not shown.

3.6 Case 6: The interaction between underwater explosion and complex solid structure with a polygonal inclusion

The whole domain is $\Omega = \{(x,y)|x \in [-6,8], y \in [-6,6]\}$ comprising of gas, water and solid. The initial setup and condition used in this case are the same as those used in Case 4, except that a polygonal solid inclusion is in the solid1 (See Fig. 19). The computation is allowed to run till 0.065.

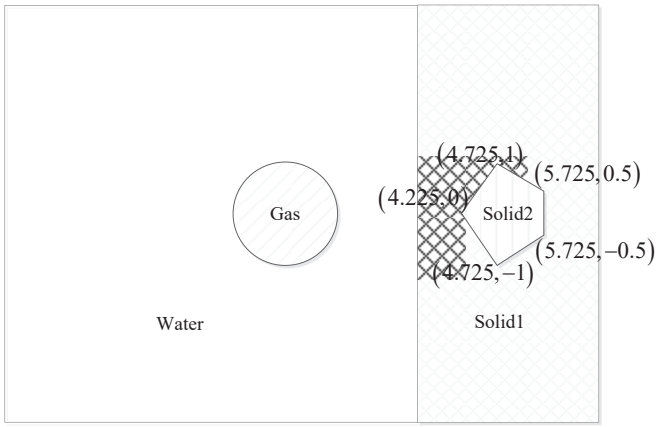
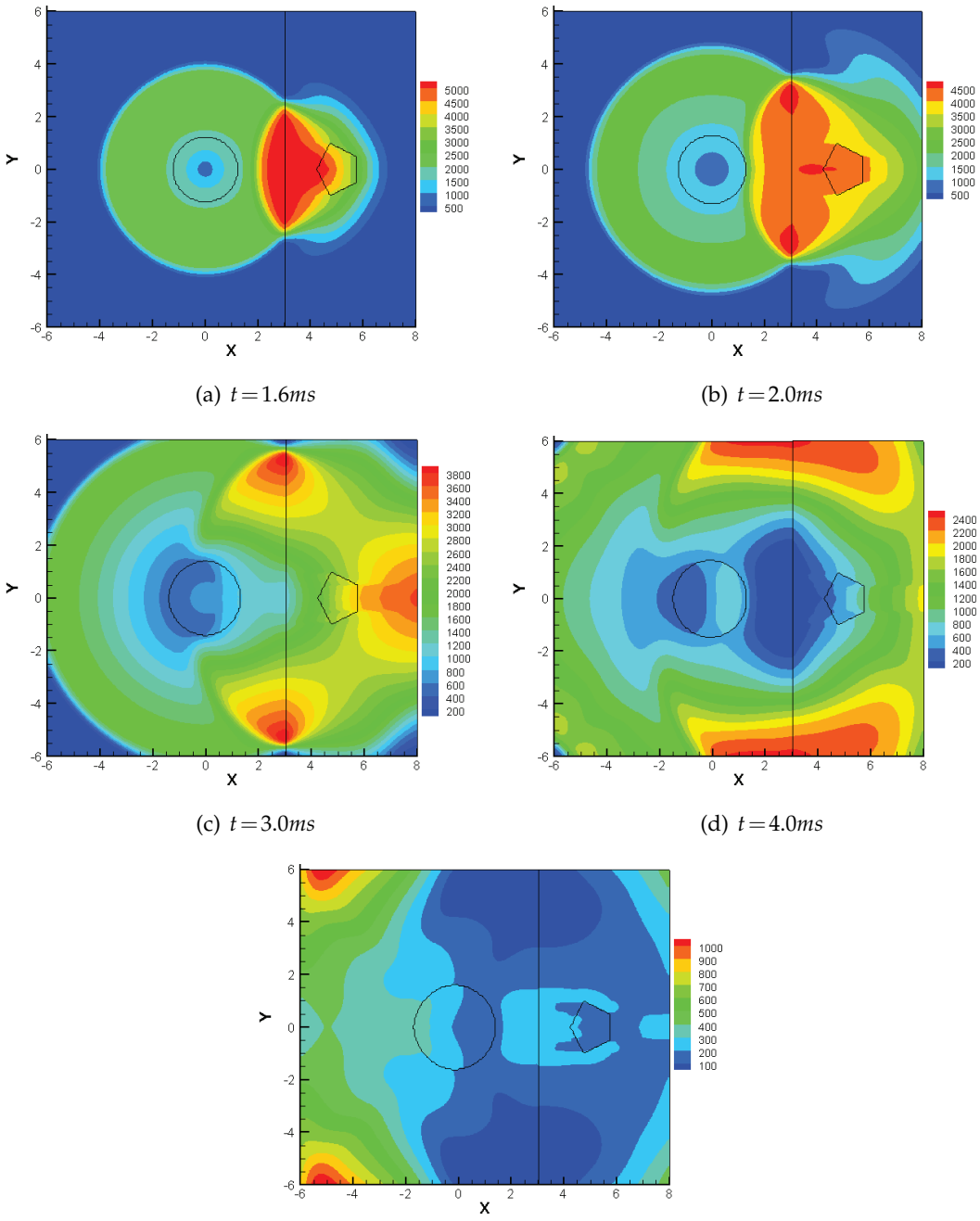


Figure 19: Schematic illustration of Case 6.

The pressure distributions (or negative stress along x-direction) at different significant instants are displayed in Figs. 20(a)-(e). The solid lines represent the bubble, the fluid-solid interface and the polygonal solid inclusion. The whole process of the interaction between underwater explosion and the solid structure is very similar to the Case 4. Here we only describe the differences caused by the polygonal inclusion. Faster loading waves inside solid2, compared with the waves in solid1, are observed in Figs. 20(a)-(b) because of the same reason as that in Case 5. As a result of the polygonal solid inclusion in solid structure, the response of solid structure subjected to underwater explosion in this case is changed (see Fig. 20). The deformation of the interfaces is similar to that in Case 5 and not shown here.

https://doi.org/10.4208/cicp.OA-2016-0212 Published online by Cambridge University Press



(a) $t=1.6ms$ (b) $t=2.0ms$

(c) $t=3.0ms$ (d) $t=4.0ms$

(e) $t=6.5ms$

Figure 20: Pressure distribution for Case 6.

https://doi.org/10.4208/cicp.OA-2016-0212 Published online by Cambridge University Press

3.7 Case 7: The interaction between underwater explosion and complex solid structure immersed in water

The whole domain is $\Omega = \{(x,y)|x \in [-6,8], y \in [-6,6]\}$ comprising of gas, water and solid. The underwater explosion is achieved by assuming a zone filled with ideal gas of high pressure and density initially located at the origin $(0,0)$ with radius $1.0m$. The surrounding water is at atmospheric pressure. A circular solid structure composed of two circular solid structures located at $(4.15,0)$ with respective radius $1.01m$ and $1.55m$ is immersed in water. Pressure equilibrium is initially across the water-solid interface. Fig. 21 provides the schematic of this case. The initial condition used in this case is the same as those used in Case 4. The computation is allowed to run till 0.043.

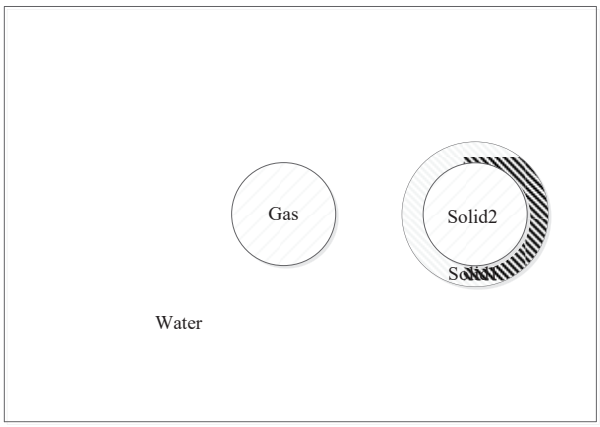
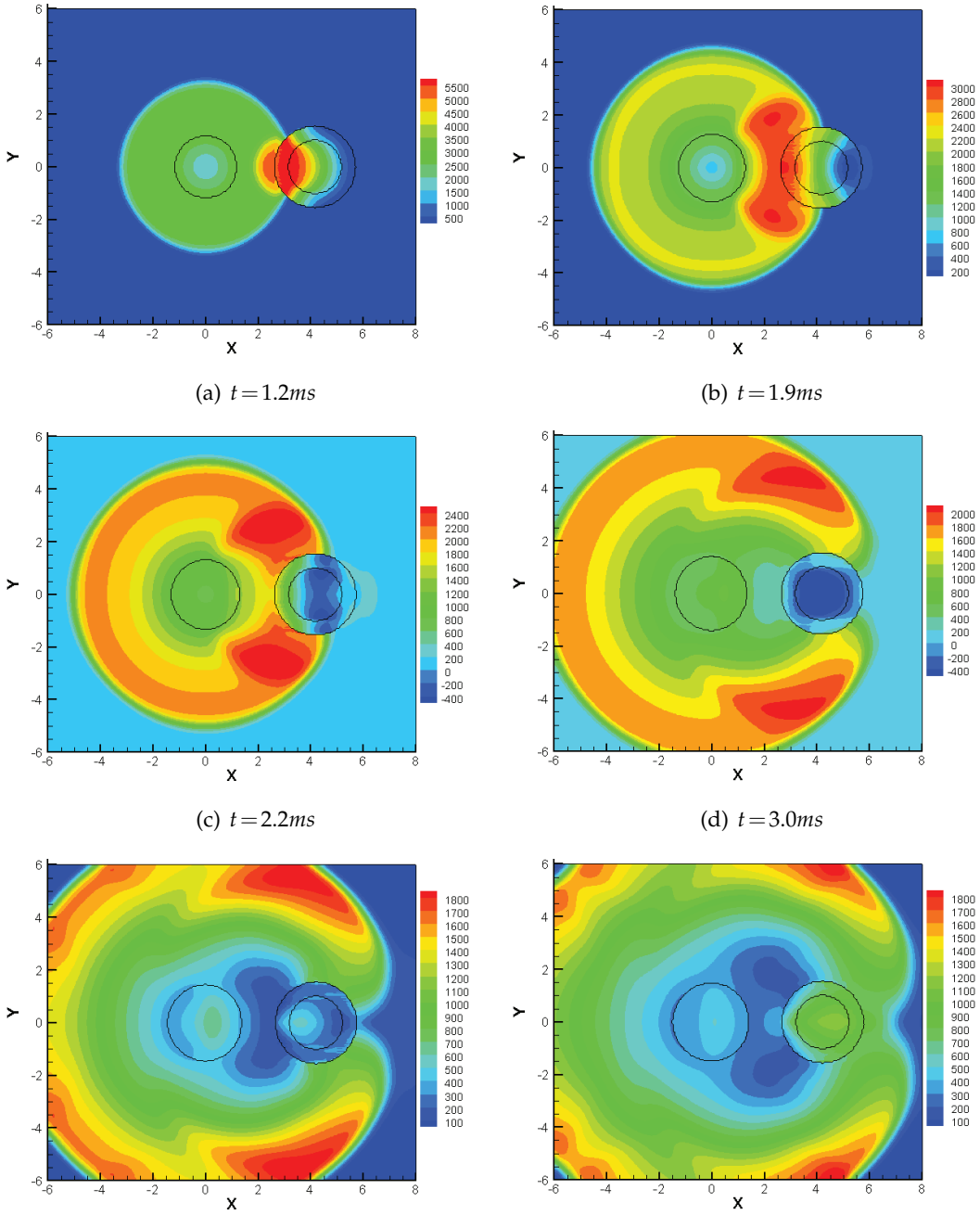


Figure 21: Schematic illustration of Case 7.

The pressure distributions (or negative stress along x-direction) at different significant instants are displayed in Figs. 22(a)-(f). The solid lines represent the bubble, the fluid-solid interface and the circular solid inclusion. When the shock wave emanating from the high pressure explosive bubble impacts the solid structure, faster loading waves inside the solid2 and slower loading waves inside the solid1 are observed in Fig. 22(a) because the Young's modulus of solid2 is bigger than that of solid1. Subsequently, the compression wave travelling in solid come to the water and shock refraction occurs at the right side of the fluid-solid interface which leads to the reflected rarefaction wave and the transmitted shock wave (see Fig. 22(b)). The reflected rarefaction waves reduce the pressure in solid continuously, which gives rise to the tensile stress in solid (see Figs. 22(c)-(d)). Afterwards, the shock waves in the water from the up and down sides of the solid meet each other as shown in Fig. 22(e). At last, the surrounding high pressure water reloads the solid (see Fig. 22(f)). The bubble interface is found to grow and the side near the solid is suppressed more slightly compared to Case 4 because the interacted solid area is very small in this case (see Fig. 22). The deformation of the water-solid interface and solid-solid interface is very slightly, which is shown.

https://doi.org/10.4208/cicp.OA-2016-0212 Published online by Cambridge University Press



(a) $t=1.2ms$ (b) $t=1.9ms$

(c) $t=2.2ms$ (d) $t=3.0ms$

(e) $t=3.53ms$ (f) $t=3.94ms$

Figure 22: Pressure distribution for Case 7.

https://doi.org/10.4208/cicp.OA-2016-0212 Published online by Cambridge University Press

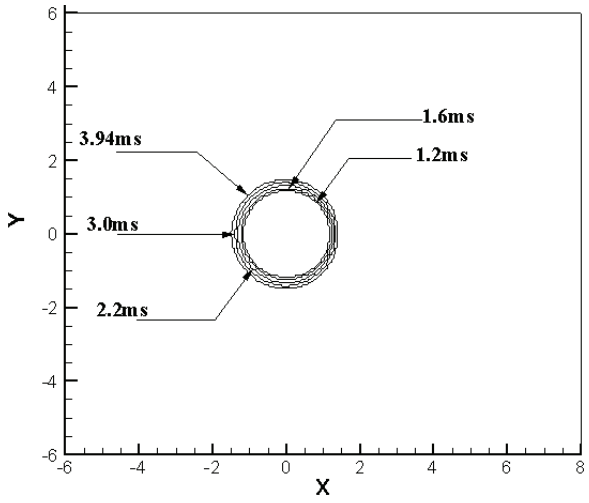


Figure 23: The evolution of the gas-water interface with respect to time.

4 Concluding remark

In this work, a consistent and coherent method based on the MGM is developed to deal with multi-medium interaction with elastic-plastic solid. This method is simpler to implement and can be used together with a single-medium solver of choice without further modifications. In this method, the compressible fluid is solved in Eulerian coordinate and the solid is solved in Lagrangian system. The method is validated by two 2D FSI problems and a 2D gas-water-solid1-solid2 interaction problem both compared with the analytic solution. Then in Case 3, the interaction between structure and underwater explosion is studied using the MGM. Furthermore, three different complex solid structures subjected to underwater explosion are simulated, respectively in Case 5-7. Numerical experiments indicate that the MGM proposed in this paper can numerically model various interactions: liquid-liquid, gas-liquid, gas-gas, fluid-solid, solid-solid interactions for the truly compressible multi-medium interaction problems involving various phases of material.

Acknowledgments

This research was supported by the Joint Fund of the National Natural Science Foundation of China and the China Academy of Engineering Physics (NSAF) (Grant No. U1530147), the National Natural Science Foundation of China (Project Nos. 11502021, 11272057) and the scholarship from China Scholarship Council (CSC) under the Grant No. 201506030042.

https://doi.org/10.4208/cicp.OA-2016-0212 Published online by Cambridge University Press

References

[1] F. H. Hamdan, Near-field fluid-structure interaction using Lagrangian fluid finite elements, Comput. Struct., 71 (1999), 123-141.
[2] S. Turek, J. Hron, M. Madlik, M. Razzaq, H. Wobker and J. Ackder, Numerical simulation and benchmarking of a monolithic multigrid solver for fluid-structure interaction problems with application to hemodynamics, Springer, 2011.
[3] K. Y. Bilah and R. H. Scanlan, Resonance, Tacoma Narrows bridge failure, and undergraduate physics textbooks, Am. J. Phys., 59 (1991), 118-124.
[4] R. Wüchner, A. Kupzok and K. U. Bletzinger, A framework for stabilized partitioned analysis of thin membrane-wind interaction, Int. J. Numer. Methods Fluids, 54 (2007), 945-963.
[5] E. Fathallah, H. Qi, L. Tong and M. Helal, Numerical investigation of the dynamic response of optimized composite elliptical submersible pressure hull subjected to non-contact underwater explosion, Compos. Struct., 121 (2015), 121-133.
[6] M. Schäfer, and I. Teschauer, Numerical simulation of coupled fluid-solid problems, Comput. Method. Appl. M., 190 (2001), 3645-3667.
[7] C. Zhang and R. J. LeVeque, The immersed interface method for acoustic wave equations with discontinuous coefficients, Wave motion, 25 (1997), 237-263.
[8] Y. Wang, C. Shu, C. Teo and J. Wu, An immersed boundary-lattice Boltzmann flux solver and its applications to fluid-structure interaction problems, J. Fluids Struct., 54 (2015) 440-465.
[9] J. C. Anderson, C. Garth, M. A. Duchaineau and K. I. Joy, Discrete Multi-Material Interface Reconstruction for Volume Fraction Data, Comput. Graph. Forum, 27, 3 (2008), 1015C1022.
[10] R. Qin and H. Bhadeshia, Phase field method, Mater. Sci. Technol., 26 (2010) 803-811.
[11] R. P. Fedkiw, T. Aslam, B. Merriman and S. Osher, A non-oscillatory Eulerian approach to interfaces in multimaterial flows (the ghost fluid method), J. Comput. Phys., 152 (1999) 457-492.
[12] T. G. Liu, B. C. Khoo and K. S. Yeo, Ghost fluid method for strong shock impacting on material interface, J. Comput. Phys., 190 (2003) 651-681.
[13] C. W. Wang, T. G. Liu and B. C. Khoo, A real ghost fluid method for the simulation of multimedium compressible flow, SIAM J. Sci. Comput., 28 (2006) 278-302.
[14] T. G. Liu, A. W. Chowdhury and B.C. Khoo, The Modified Ghost Fluid Method Applied to Fluid-Elastic Structure Interaction, Adv. Appl. Math. Mech., 3 (2011) 611-632.
[15] A. Kaboudian and B. C. Khoo, The ghost solid method for the elastic solid-solid interface, J. Comput. Phys., 257 (2014) 102-125.
[16] A. Kaboudian, P. Tavallai and B. C. Khoo, The ghost solid methods for the elastic-plastic solid-solid interface and the theta-criterion, J. Comput. Phys., 302 (2015) 618-652.
[17] L. Xu and T. Liu, Accuracies and conservation errors of various ghost fluid methods for multi-medium Riemann problem, J. Comput. Phys., 230 (2011) 4975-4990.
[18] Y. Chen and S. D. Heister, A numerical treatment for attached cavitation, J. Fluids Eng., 116 (1994) 613-618.
[19] X. Lin, Numerical computation of stress waves in solids, Vch Pub, 1996.
[20] F. Cirak and R. Radovitzky, A Lagrangian-Eulerian shell-fluid coupling algorithm based on level sets, Comput. Struct., 83 (2005) 491-498.
[21] S. Osher and R. Fedkiw, Level set methods and dynamic implicit surfaces, Springer Science & Business Media, 2006.
[22] U. Kuttler and W.A. Wall, Fixed-point fluid-structure interaction solvers with dynamic relaxation, Comput. Mech., 43 (2008) 61-72.

https://doi.org/10.4208/cicp.OA-2016-0212 Published online by Cambridge University Press

[23] T. G. Liu, J. Y. Ho, B. C. Khoo and A. W. Chowdhury, Numerical simulation of fluid-structure interaction using modified Ghost Fluid Method and Naviers equations, J. Sci. Comput., 36 (2008) 45-68.
[24] J. R. Davis, Concise metals engineering data book, Asm International, 1997.
[25] P. M. Michaelsen, B. Pritz and M. Gabi, A Fluid-Structure-Interaction tool by coupling of existing codes, Proceedings of the 20th European MPI Users' Group Meeting. ACM, (2013) 157-162.

https://doi.org/10.4208/cicp.OA-2016-0212 Published online by Cambridge University Press